

MIT Open Access Articles

*NICER instrument detector subsystem:
description and performance*

The MIT Faculty has made this article openly available. **Please share** how this access benefits you. Your story matters.

Citation: Prigozhin, Gregory, et al. "NICER Instrument Detector Subsystem: Description and Performance." Proceedings Volume 9905, Space Telescopes and Instrumentation 2016: Ultraviolet to Gamma Ray, 26 June - 1 July, 2016, Edinburgh, United Kingdom, edited by Jan-Willem A. den Herder et al., SPIE, 2016, p. 99051I. © 2016 SPIE.

As Published: <http://dx.doi.org/10.1117/12.2231718>

Publisher: SPIE

Persistent URL: <http://hdl.handle.net/1721.1/117024>

Version: Final published version: final published article, as it appeared in a journal, conference proceedings, or other formally published context

Terms of Use: Article is made available in accordance with the publisher's policy and may be subject to US copyright law. Please refer to the publisher's site for terms of use.



PROCEEDINGS OF SPIE

[SPIDigitalLibrary.org/conference-proceedings-of-spie](https://spiedigitallibrary.org/conference-proceedings-of-spie)

NICER instrument detector subsystem: description and performance

Gregory Prigozhin, Keith Gendreau, John P. Doty, Richard Foster, Ronald Remillard, et al.

Gregory Prigozhin, Keith Gendreau, John P. Doty, Richard Foster, Ronald Remillard, Andrew Malonis, Beverly LaMarr, Michael Vezie, Mark Egan, Jesus Villasenor, Zaven Arzoumanian, Wayne Baumgartner, Frank Scholze, Christian Laubis, Michael Krumrey, Alan Huber, "NICER instrument detector subsystem: description and performance," Proc. SPIE 9905, Space Telescopes and Instrumentation 2016: Ultraviolet to Gamma Ray, 99051I (18 July 2016); doi: 10.1117/12.2231718

SPIE.

Event: SPIE Astronomical Telescopes + Instrumentation, 2016, Edinburgh, United Kingdom

NICER Instrument Detector Subsystem: Description and Performance

Gregory Prigozhin^a, Keith Gendreau^b, John P. Doty^c, Richard Foster^a, Ronald Remillard^a, Andrew Malonis^a, Beverly LaMarr^a, Michael Vezie^a, Mark Egan^a, Joel Villasenor^a, Zaven Arzumian^{bf}, Wayne Baumgartner^b, Frank Scholze^d, Christian Laubis^d, Michael Krumrey^d, and Alan Huber^e

^aMIT Kavli Institute for Astrophysics, Cambridge, MA, USA

^bNASA Goddard Space Flight Center, Greenbelt, MD, USA

^cNoqi Aerospace, Pine, CO, USA

^dPhysikalisch-Technische Bundesanstalt, Berlin, Germany

^eAmptek, Bedford, MA, USA

^fCRESST, Universities Space Research Association, Columbia MD, USA

ABSTRACT

An instrument called Neutron Star Interior Composition Explorer (NICER) will be placed on-board the International Space Station in 2017. It is designed to detect soft X-ray emission from compact sources and to provide both spectral and high resolution timing information about the incoming flux. The focal plane is populated with 56 customized Silicon Drift Detectors. The paper describes the detector system architecture, the electronics and presents the results of the laboratory testing of both flight and engineering units, as well as some of the calibration results obtained with synchrotron radiation in the laboratory of PTB at BESSY II.

Keywords: Silicon Drift Detectors, X-rays, spectroscopy, calibration

1. INTRODUCTION

NICER is an instrument that has recently been built at NASA Goddard Space Flight Center and now awaits to be deployed on the International Space Station. According to the current plan it is scheduled to be launched in February 2017. The detailed description of the entire instrument is given in [1]. The goal of the instrument is to detect soft X-ray emission (0.2 – 12 keV) from neutron stars and other celestial sources with unprecedented timing resolution of about 100 ns. The focal plane is comprised of 56 Silicon Drift Detectors (SDD) manufactured by Amptek [2]. SDDs are commonly used as soft X-ray spectroscopic sensors; thus, the instrument will be capable of providing spectral information in addition to precise timing of each detected photon. Each detector has its own compact X-ray focusing optics in front of it (so-called concentrators), and all mirror-detector pairs are coaligned to look at the same object, providing large collection area. The main goal of the instrument is to monitor temporal and spectral variability of very compact X-ray sources. SDDs are in essence single pixel detectors, thus, primary observational targets are celestial point sources, for which imaging is not important.

In this paper we will describe the NICER detector system, including the detectors themselves and the main features of the electronics that controls the detectors, and the results of the tests performed up to date demonstrating the level of performance of the instrument.

2. DETECTOR SUBSYSTEM ARCHITECTURE

The detector subsystem consists of the 56 Focal Plane Modules (FPMs) arranged into a 7 x 8 array, and the electronics that controls them. An individual FPM includes the Amptek Silicon Drift Detector mounted onto a small board with a preamplifier and is enclosed into a metal housing that is bolted to the metal plate at the focal plane of the instrument.

Further author information: (Send correspondence to G.P.)

G.P.: E-mail: gyp@space.mit.edu

2.1 Focal Plane Modules

The FPM is built around the Amptek FAST SDD, a 500 micron thick detector mounted on top of the Thermo-Electric Cooler (TEC). The TEC cools the detector to a nominal (for NICER) temperature of -55°C , in order to suppress dark current in the large volume of fully depleted silicon. Both the silicon chip and the TEC are enclosed within the hermetically sealed metal can of a TO-8 package with a very thin custom-made entrance

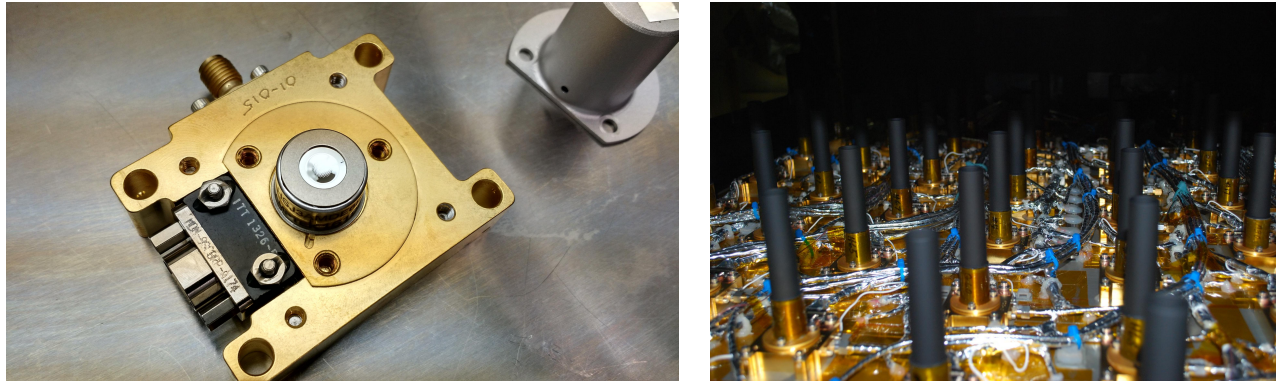


Figure 1. Left: A single Focal Plane Module - a detector can is attached to the gold plated housing. Right: A view of the portion of the actual instrument focal plane, detectors are hidden inside the cones that protect them from background radiation and stray light.

window. The window is made out of a 40 nm Silicon Nitride film covered by 30 nm of Aluminum that blocks visible light. Such a window has very high transmission even at low energies, about 30% at 200 eV, as measured at the synchrotron facility. A picture of the assembled FPM is shown on Fig. 1. A shiny slightly concave surface at the center of the detector is the thin optical blocking window.

It is somewhat unusual to use SDD as a timing detector, because electron drift time depends on the distance from the photon interaction site to the detector anode, and this distance varies substantially across the detector. To be able to use SDD as a timing sensor it was decided to reduce the area of the active detector surface, which helped to keep drift times in a relatively tight range. In off-the-shelf Amptek detectors the periphery of the 25 mm^2 active area is shielded by the internal multilayer collimator that prevents X-rays from illuminating the area with poor collection efficiency far from detector center. For NICER, the collimator was modified to have a small 2 mm diameter opening in the center. The X-ray optics in front of the SDD have a Point Spread Function smaller than this opening and the shielded device periphery serves as a background rejection volume. The background rejection algorithms are explained below in section 3.4.

Amptek's FAST SDD includes a built-in CMOS preamplifier mounted inside the package very close to the detector chip itself. This results in a small load capacitance at the detector output and lower noise and higher speed than for regular SDDs. To bias the detector to its normal mode of operation with fully depleted volume, a -130 V bias is provided by an MPU (Measurement and Power Unit). The FPM includes a small printed-circuit board (it is not visible in the photograph, being hidden inside the metal housing) with a simple opamp gain stage that is designed to drive a relatively long 50 Ohm coax cable that connects the FPM output to the input of the MPU. The gain of the entire FPM is approximately 4.8 mV per keV of deposited photon energy. The FPM board also contains a circuit which resets the detector anode to the ground potential as soon as the detector output level reaches +2.0 V. A typical reset period at a nominal temperature is found to be in the range 0.3-0.5 seconds for flight detectors. An example of the signal shape at the output of the FPM is shown on Fig. 2. A sharp voltage drop is caused by reset pulse restoring potential at the detector anode. The slow rise is due to dark current generated across the detector volume. The reason for the slightly increased slope immediately before the detector reset is a nonlinear behavior of the built-in CMOS preamplifier near the top of its range, but our testing of X-ray performance verified that it has no measurable effect on any of the detector parameters – the time scale of this distortion is hundreds of milliseconds, orders of magnitude larger than the time constants of the pulse shaping circuits.

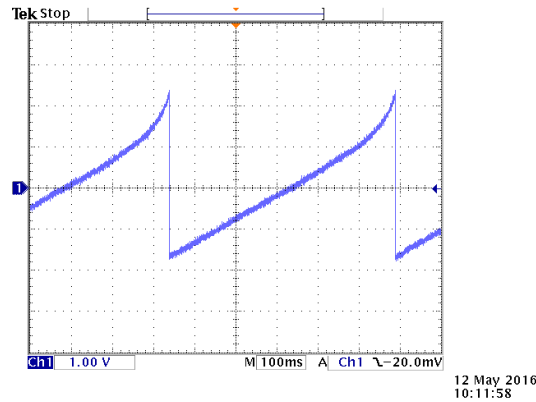


Figure 2. Shape of the signal at the output of the FPM. A rising ramp is due to dark current slowly discharging detector anode. Once the voltage reaches the level of 2.0 V, a reset pulse returns the detector anode to the ground potential.

2.2 Electronics

The 56 detector units comprising the focal plane are divided into 7 groups of 8 FPMs, each group being controlled by an independent set of electronics, the so-called MPU slice. An MPU slice is powered by a single +28 Volt supply line provided by the Main Electronics Box (MEB). MEB is not considered to be part of the detector system and is beyond the scope of this paper. The +28 V power is immediately filtered and downconverted by International Rectifier Power Modules to +3.3V, +5V and -5V supplies which are used by the MPU circuits. Each MPU slice is divided in 2 boards: digital and analog. They have the same size and are mounted on top of each other via interboard connectors. We will describe each board's functions in the following two subsections.

2.2.1 Digital board

A functional diagram of the digital board is shown in Fig. 3. Each slice has its own ARM-based microcontroller,

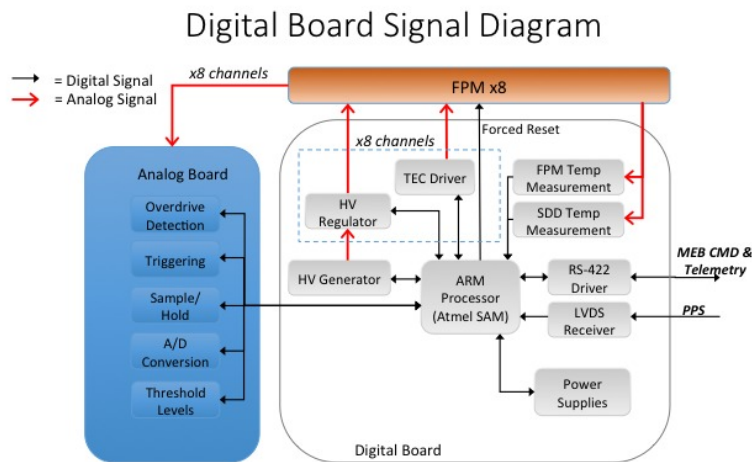


Figure 3. Digital board functional diagram.

an ATMEL AT91SAM7A3, which orchestrates all the operations of the group of 8 detectors. This is the key part of the digital board. An 18.432 MHz crystal oscillator provides a clock that is used by the microcontroller's PLL circuit to generate a higher frequency master clock (the frequency is multiplied by 28 and divided by 5 and then 4) with a period of 38.75 ns. This is a tick unit utilized for time tagging the signals within a given slice.

The counter keeps track of the number of ticks since the slice was turned on and for every registered trigger its tick count is reported.

Each slice is connected to the Main Electronics Box via an RS-422 interface, through which commands are sent to the MPU slice, and data containing information about the amplitudes and times of arrival of each registered photon, as well as housekeeping information, flow in the opposite direction from the MPU to the MEB. The RS-422 connection limits the data rate that can be transferred from a single slice to approximately 5520 photons/second, once all the extra bits are taken into account. The same 9-pin connector used for RS-422 interface also brings in the PulsePerSecond (PPS) signal in LVDS format that every second provides the MPU slice with a time reference from the on-board GPS. The microcontroller determines and reports the tick count for each PPS, which helps to continuously track photon timing in absolute units.

The microcontroller performs a multitude of signal processing tasks such as time-stamping the X-ray events, handling the digitized photon amplitudes registered by the analog circuits, packaging X-ray events and housekeeping information into the CCSDS format, and sending those packets to the MEB via the RS-422 line.

The digital board generates high voltage to bias the SDD electrodes. The nominal level is -130 V, but it can be changed by setting a control DAC to a different level. The high voltage (HV) is generated by a single eight stage Cockroft-Walton voltage multiplier, which then branches out into 8 separate voltage regulators, one per FPM, that reduce the ripples and allow independent settings of HV for each detector.

Another important function of the digital board is controlling the temperature of the SDDs. The board has 8 independent low-dropout linear regulators powered by 3.3V line that provide current to 8 TECs maintaining SDD temperature individually. The regulator circuit is shown in Fig 4. Every SDD has a temperature sensing diode mounted very close to it, on the same ceramic board attached to the cold side of the TEC. The voltage drop across each of the 8 diodes is measured as 100 μ A forward biasing current is pushed sequentially through all of them, providing a temperature reading for each SDD. The feedback loop that keeps the SDD at the desired

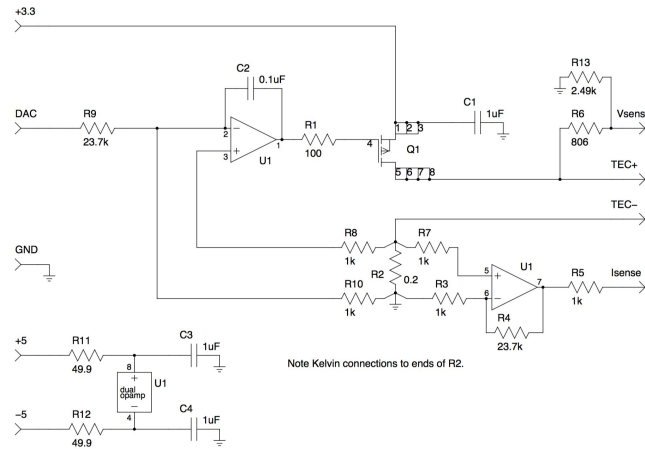


Figure 4. Low dropout linear regulator controlling the Thermo-Electric Cooler.

temperature is closed via the microcontroller, which reads each temperature every second and sets the DAC value that controls the current flowing into the TEC using a classic PID algorithm running in the processor. Typical time of initial temperature settling is from 2 to 4 minutes.

2.2.2 Analog board

The analog board's main function is to process signals coming from the FPMs, to detect events, and measure the amplitude and time of arrival of a voltage step that represents an X-ray absorbed inside the body of an SDD. It has 8 identical channels, one per FPM. All of the channels feed a single Analog-to-Digital Conversion (ADC) chip common for all channels. Each channel includes two parallel shaper circuits, one "slow", with 465 ns peaking time, and another "fast", with 84 ns peaking time, as shown in the analog board functional diagram in

Analog Board Signal Diagram

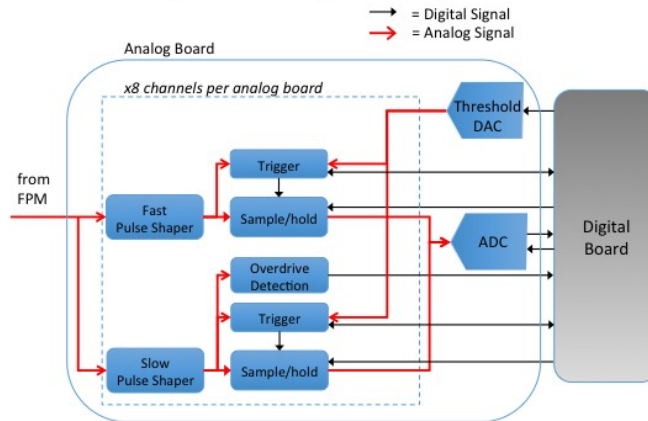


Figure 5. Analog board functional diagram.

Fig. 5. The primary purpose of the shaping circuits is the removal of high frequency noise present in the detector signal coming from the FPM. The slow shaper, with narrower passband, is more effective in noise reduction, thus resulting in more accurate amplitude detection and superior spectral performance. The slow chain is always used for extracting spectral information. The fast chain, with much wider passband, includes higher frequency components which produce better timing accuracy, and it is the primary source for time stamps of the X-ray events. One caveat here is that fast chain has higher read noise level, and because of that it cannot detect events near low energy end of the spectrum. For such events timing information from the slow channel is used and timing offset between the chains has to be accounted for. This offset can be clearly seen and measured in the calibration results shown later in Fig. 7.

There is another important role that the fast chain plays in data analysis: it helps in rejecting events that originate far from the detector center. This is based on the ballistic deficit phenomenon (amplitude reduction for a slow-rising signal, see [3]) and is described in more detail below in section 3.4.

Both fast and slow shapers have the same circuit diagram, shown in Fig. 6 for the fast shaper. The slow shaper has proportionally larger capacitor values. The circuit is a three stage Bessel filter with proportional unipolar output called "outu" and bipolar "outb", with outb being an output of differentiating stage. The delays

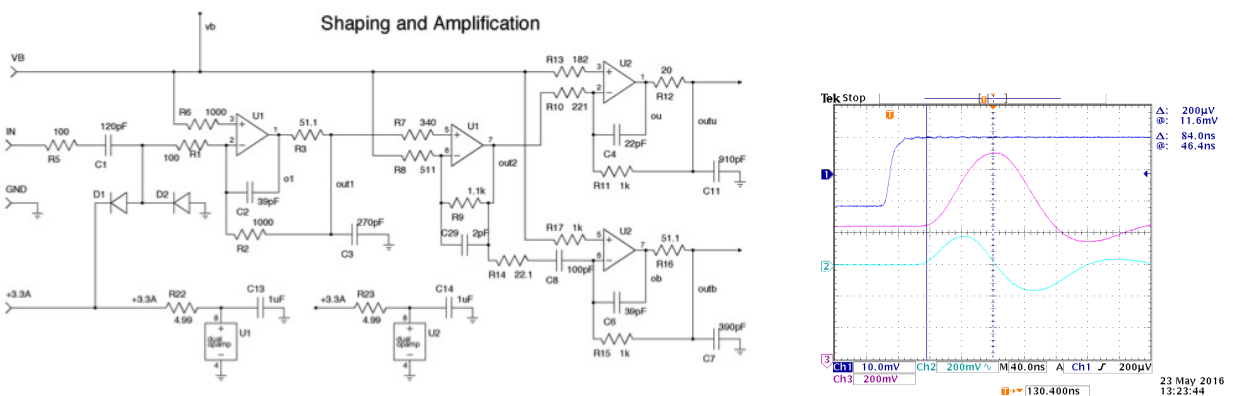


Figure 6. Left: Shaper circuit for fast chain. Right: oscilloscope shot of input step (blue), unipolar shaper output *outu* (purple), and bipolar shaper output *outb* (green). Zero crossing of *outb* corresponds to the max of *outu*.

are adjusted for *outb* zero crossing to correspond to the time of *outu* signal peaking. This is used for amplitude capture: *outb* first arms the triggering circuit once its level exceeds predetermined programmable threshold, and then, at zero crossing, an impulse is produced that latches the value reached by *outu*, which represents the amplitude of the X-ray event. The rising edge of this impulse marks the time of the event arrival, it is sent to the microcontroller timing input and is latched there. There is some additional fast logic in the way (not shown), deciding whether to use fast or slow trigger for timing (as explained above, for low energy events the fast trigger may not happen, in this case the slow trigger time is used).

The latched amplitudes of *outu* in both fast and slow chains are digitized sequentially by the same ADC, an 18 bit very low power AD7982. Only the 12 most significant bits are used to report amplitude values to the microcontroller. Both slow and fast amplitude values are included in the event parameters that are sent to the ground for each detected trigger to be used later in the analysis for background rejection.

Signal amplitude latching design includes what we call a "Forced Trigger" circuit that allows to latch the amplitude level in the absence of a normally triggered event by issuing a command. That turns out to be an extremely useful feature helping to measure circuit noise properties and the digital offset corresponding to zero amplitude signal.

The slow chain also has overdrive detection circuits. They send a signal to the microcontroller to report the arrival of the event whose amplitude exceeds approximately 18 keV. Such events are marked with a "positive overdrive" flag. Most particle events would fall into this category and could be easily rejected. There is another flag for "negative overdrive" which is set if the signal amplitude is negative and exceeds a preset value. This happens when the detector reset (which is a negative step of the signal) occurs, marking the resets and their time of arrival with a specific flag. This is very useful for many purposes, including, for instance, simple liveness tests with no source present.

3. PERFORMANCE

In this section we will describe different aspects of the detector performance with each subsection dealing with a separate set of parameters.

3.1 Timing

We used a Modulated X-ray Source (MXS), described in [4], to test both timing and spectroscopic properties of the flight detectors. As part of the calibration process, 8 detectors were mounted on a baseplate and illuminated by the MXS inside a vacuum chamber. The MXS was driven by a series of 20 ns long pulses at 600 kHz frequency, produced by a very stable function generator with ovenized crystal oscillator. The train of pulses was synchronized with the PPS signal providing time stamps to the MPU. The MXS was installed in such a way that emitted X-rays illuminated a secondary fluorescence target containing Carbon, Fluorine, Aluminum, Titanium and Copper. As a result, the spectrum seen by the tested detectors contained only the characteristic X-ray lines of those elements with no contamination from continuum.

A density plot of X-ray events registered by the MPU during a typical calibration run is shown on Fig. 7. The energy of the photons is shown on the x-axis, while the y-axis shows the time stamps of events, folded over the period of the clock that modulates the X-ray source. Each vertical streak in the figure corresponds to one of the characteristic lines emitted by the X-ray source. The centroid and width of each streak (in vertical direction) represent, correspondingly, the delay time and timing uncertainty for the signal detected by the MPU. On the time axis all different energies are very well aligned, indicating that detector system timing is not energy dependent when time detection is done by the fast chain. At low energies time detection is performed by the slow chain which creates a shift in time stamping, which can be seen for the lowest energy line (Carbon at 277 eV) at the very left of Fig. 7. This time shift will be compensated, once the detector calibration is completed.

Another powerful test of timing properties of the NICER detectors came as a byproduct of the detector calibration in the PTB laboratory at the synchrotron radiation facility BESSY II [5]. Since electrons in the synchrotron storage ring make a full revolution in 800 ns, and are injected into the ring in very short bunches of a certain predetermined pattern, that pattern can be detected by the devices under test, if they have good enough time resolution. The result of processing of the time stamps of the X-ray events returned by the MPU

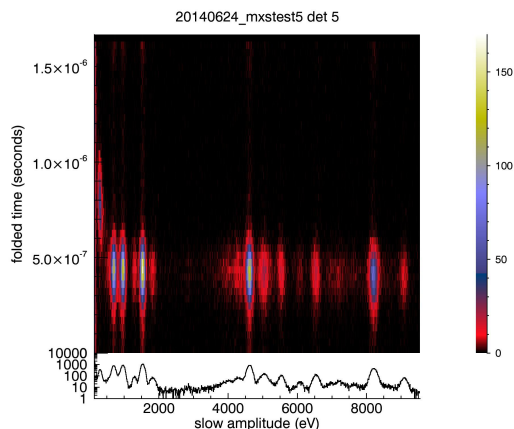


Figure 7. Events density plot for the data acquired with the pulsed X-ray source. The X-axis is the amplitude of the events in the slow chain of the MPU, the y-axis is the event time of arrival, as registered by the MPU.

is shown below in Fig. 8. The processing involved finding a periodicity in the stream of data using an FFT (Fast Fourier Transform), and then folding the time over the found period. Since the clock we used during the synchrotron run was not very accurate, in the data processing we had to divide data in relatively short intervals of about 0.5 seconds and repeat the procedure of computing an FFT and time folding for each interval, then cross-correlate the time histograms for each of them against the others. The cross correlation could also be done

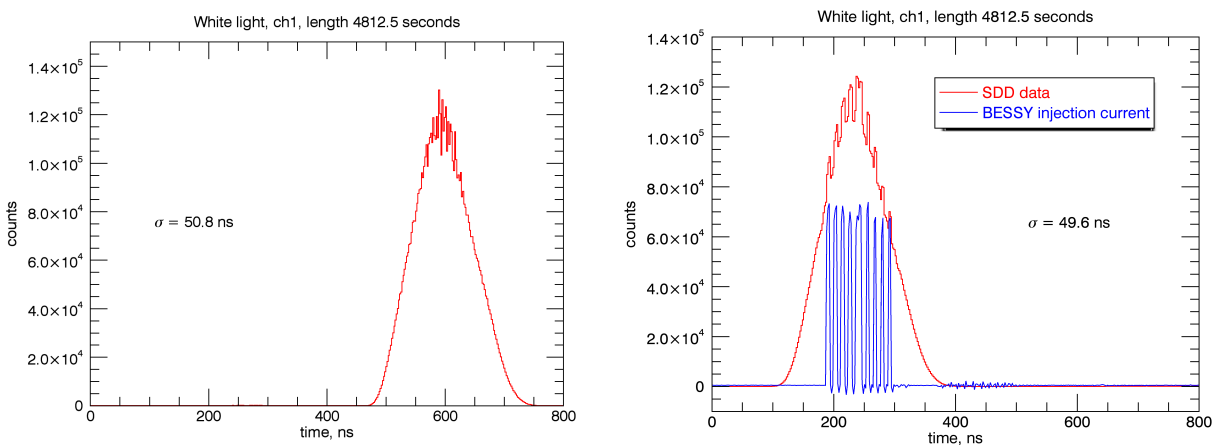


Figure 8. SDD timing. Histograms of photon time of arrival, as registered by the MPU, with time folded over the period of electrons travelling around the electron storage ring (800 ns). Left plot - no prior knowledge was assumed about the timing of the beam except its periodicity. Right plot: data processing incorporated cross-correlation with known injection current pattern. The peaks are in different locations because in the self-correlation case the position is determined by a random position of the very first chunk of data.

with the known synchrotron ring injection pattern, rather than with the folded profile from the adjacent portions of the data. Both results are shown in Fig. 8, and, as expected, cross-correlation with the known underlying pattern brings out the details of the source timing variability with an astonishing precision (right plot in Fig. 8). The width of the time histogram is remarkably small, only 49.6 ns (measured as a σ of the best-fit gaussian). This measurement has been done at the so-called white light beam, with undispersed bending magnet radiation. The beam was confined in this case by two rectangular slits to the size of 1 mm x 1 mm, with the center of the square aligned with the detector center. Reduced size of the illuminated spot helped to keep timing dispersion

smaller. Such tight timing histogram confirms that detected timing is energy independent, a very important property of the flight instrument.

3.2 Quantum Efficiency

Two detectors selected from the original flight lot were designated as reference detectors. These detectors were used in every calibration run along with 6 other flight detectors mounted on the same backplate when data were acquired during long exposures to the MXS illumination. This way every flight detector has its efficiency calibrated against the reference detectors. Once this calibration was accomplished, both reference detectors were taken to BESSY II for absolute Quantum Efficiency (QE) calibration.

The calibration at BESSY II consisted of several parts. Here we will present only the results of measurements at low energies at the SX700 plane-grating monochromator beamline. During this measurement the beam size was confined by the aperture at the output of the SX700 monochromator to a spot of 0.7 mm x 0.7 mm and the spot was centered, judged by the detector response. Such spot size was well within the 2 mm diameter of the SDD collimator. For this measurement the ring current first was set to a low value of 10 mA and a photodiode, which was previously calibrated against a cryogenic electrical substitution radiometer [6], was placed in front of the SDD, intercepting the beam, and the photon flux was measured at all predetermined energies of interest. Then the calibrated photodiode was moved out of the beam, and the SDD was exposed. This level of ring current, adequate for the measurements with the photodiode, is too high for the SDD. Accordingly, the ring current was reduced down to approximately 0.1 μA to achieve flux level corresponding to about 2000 counts per second at the output of the tested SDD. At this level of illumination a substantial number of counts was accumulated at each energy point. The quantum efficiency was calculated by scaling the corresponding beam current values and data acquisition times. The result of the measurement is shown in Fig. 9 as red diamonds.

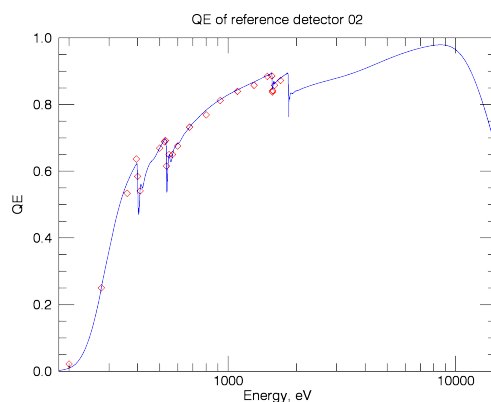


Figure 9. Quantum efficiency of the SDD as measured at the PTB's SX700 monochromator beamline (red diamonds). Overplotted (blue solid line) is simulated QE taking into account the transmission of the entrance window and the trigger efficiency effect.

Originally, the sharp drop at low energies (below 300 eV) was assumed to be due to absorption losses in the entrance window which consists of Silicon Nitride film covered by a thin Aluminum layer that blocks visible light. The transmission of the entrance window of the NICER detectors was also measured at BESSY II to a very good accuracy. Simulations indicated that window transmission alone is not enough to account for the slope of the low energy cut-off, there must be an additional factor contributing to that. It was established that the steeper-than-expected drop was caused by what we call "trigger efficiency" effect. It is described in the following subsection 3.2.1.

3.2.1 Trigger Efficiency Effect

The NICER analog readout shaping circuits (both slow and fast chains) have relatively short peaking times in order to provide accurate time stamping of the incoming X-ray photons. That results in somewhat higher noise

levels than those in typical spectroscopic applications. Also, for better timing performance – to avoid timing errors due to energy-dependent time walk, we used bipolar shaping with a differentiating chain (signal *outb* in the schematics in Fig. 6) as an input to the threshold discriminator in both slow and fast channels. As a result of superposition of several sources of noise along the path, the signal arriving at the input of the threshold discriminator, even if the detector input is a monochromatic feature, will have a probability distribution which can be represented as a gaussian function with nonzero width. The threshold discriminator will trigger on all signals with amplitude exceeding threshold value, as illustrated in Fig. 10. Thus, when the signal amplitude is

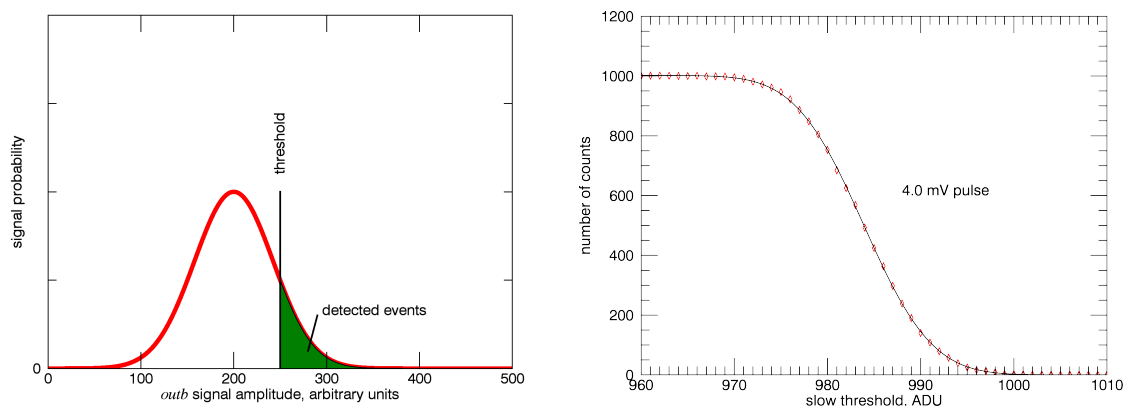


Figure 10. Left: Probability distribution of an *outb* signal amplitude at the input of the threshold discriminator, illustrating a concept that the detected events fraction should follow an error function when the *outb* amplitude is close to the threshold level. Right: experimental data showing the fraction of detected events as a function of the threshold value with a constant input signal and nearly perfect fit to an error function.

close to the threshold value, only a fraction of the events corresponding to signal values above the threshold would be detected. An illustration in Fig. 10, left, indicates that the efficiency of detection of those events (we call it "trigger efficiency") can be described by an error function. That was confirmed in multiple experiments, one of the results is shown on the right of the Fig. 10. In this case a constant 4 mV pulse was fed to the input of the MPU at a frequency of 1000 pulses per second, and the fraction of detected events is plotted as a function of the threshold. A solid line representing a best-fit error function demonstrates that this functional form describes the result extremely well. In this case the input signal is produced by a pulser, and the detector noise is excluded. The effect can be also observed in X-ray data with the detector connected, and, in fact, it is a factor that determines low energy limit of the detector. The corresponding results with the detector illuminated by X-rays at BESSY II are shown in Fig. 11. In this case the detector was exposed to undispersed synchrotron radiation (so-called "white light") and again, an error function describes the low energy efficiency cut-off extremely well. Reducing the threshold value shifts the mid-point of the error function towards lower energies in full agreement with the model, but, it also increases intensity of noise peak seen in the left part of the plot on Fig. 11 and centered around 130 eV. The noise peak intensity does not depend on the X-ray intensity, just on the threshold value, and, in principle, it means that the optimal threshold value depends on the source intensity in the low energy part of the spectrum. In practice, though, NICER is expected to operate at a nominal threshold value individually determined for each FPM. An accurate trigger efficiency model is going to be an important part of data analysis, a complicating factor being its dependence on the MPU analog board temperature.

3.3 Spectral performance

The detector system uses the slow chain of the shaper for extracting the spectral composition of the incoming X-ray flux. The most comprehensive characterization of spectral performance was done at BESSY II, where 2 reference detectors were illuminated by monochromatic X-rays across almost the entire bandwidth of the system, from 200 eV to 8048 eV. The data were taken at the SX700 beamline for energies below 1700 eV, and at the Four-Crystal Monochromator (FCM) beamline for the higher X-ray energies. Two examples of the detector response at 677 eV and 5898 eV are shown in Fig. 12. A peak centered around 130 eV in both histograms is

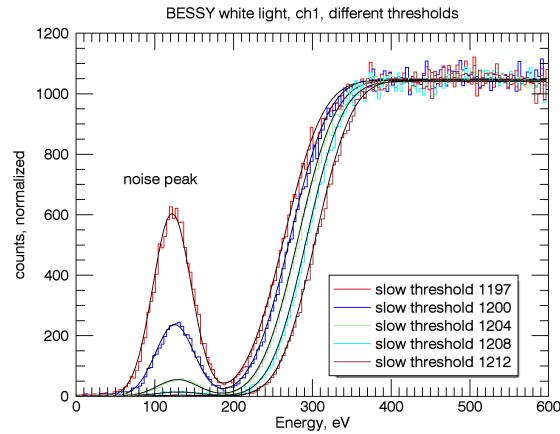


Figure 11. Detector response at the white light beamline at BESSY II at different values of the threshold. The curves were scaled to have the same value around 500 eV, thus the y-axis is labeled as normalized. Reducing the threshold moves the "trigger efficiency" curve to the left, improving the low energy response, but at the same time increases intensity of the noise peak.

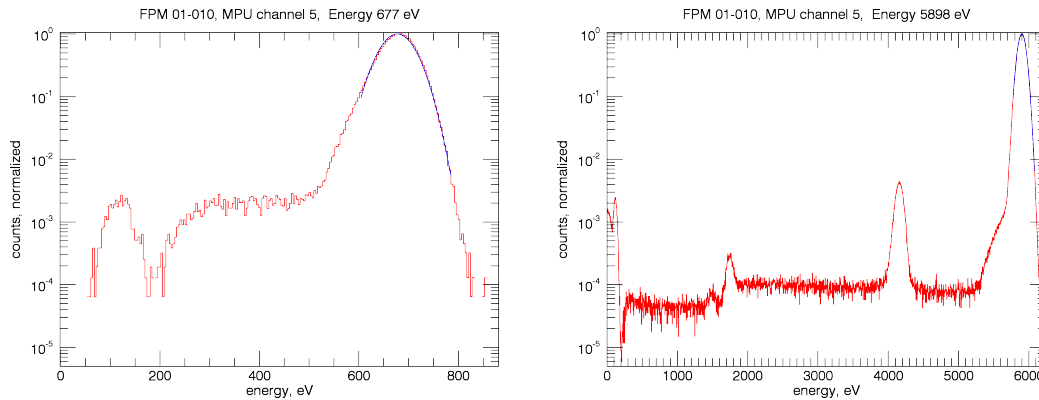


Figure 12. SDD response to monochromatic illumination, 677 eV (left) and 5898 eV (right).

a noise peak, similar to the ones shown on Fig. 11. The low energy cut-off of the low energy tail around 200 - 300 eV is due to the trigger efficiency effect, described in the section 3.2.1. In the 5898 eV histogram the silicon escape and silicon line peaks are clearly visible at 4159 eV and 1739 eV respectively. Interestingly enough, silicon line in the response is due to fluorescence from the detector entrance window, which is supported by silicon mesh. This conclusion was established by comparing the response of a windowless detector to the response of the flight ones. The very weak aluminum line just below silicon has the same origin, being fluoresced from aluminum light-blocking layer in the entrance window. For the main peaks in each of the spectral histograms a fit to a gaussian was made within a small window around the peak value (the gaussians are shown in blue in Fig. 12). A plot of the gaussian widths as a function of energy is shown on Fig. 13 as red diamonds, along with a green line that represents the common assumption that the energy resolution is a sum in quadrature of the readout noise N (in electrons rms) and a Fano noise term EF/w (E here is photon energy in eV). We assumed Fano factor $F=0.114$ and average energy per electron-hole pair $w=3.71$ eV at -55° C (see [7]). The best fit to the data produces readout noise of 8.7 electrons rms. It is interesting that at the lowest energies of 200 eV and 277 eV, the energy resolution appears to get noticeably better, while usually it tends to get worse due to charge losses near the detector surface, as X-ray penetration depth becomes very small at low energies. The real reason behind this anomalous behavior is the trigger efficiency effect, described above (section 3.2.1). The sharp loss of detection efficiency at lower energies leads to lost counts on the low energy side of the main peak of the response

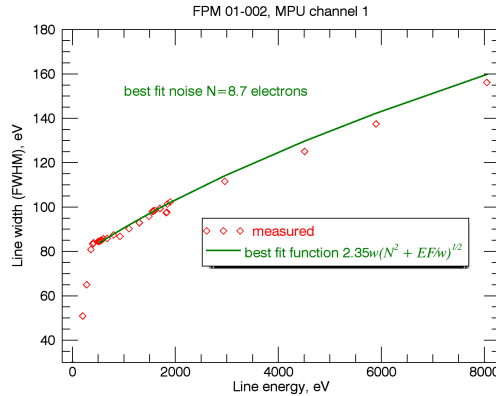


Figure 13. Energy resolution as a function of energy for the reference detector 01-002 measured at BESSY II.

histogram, distorting its shape, making it narrower, and shifting its center, in full agreement with our trigger efficiency model. We did not use these data points when fitting to find the readout noise.

3.4 Background rejection

Once in space, the SDD will produce event triggers from sources other than the X-rays arriving from the observed target and focused by the concentrator in front of the detector. X-rays coming through the concentrator optics are confined to a 2 mm diameter central spot, a limit set by a multilayer collimator placed on the surface of the SDD. There will be also a component due to diffuse cosmic X-ray background, expected to be subtracted via in-flight calibration products. The SDD, however, will also react to energetic particles and gamma rays that can easily penetrate shielding layers around the detector and can produce signal charge anywhere in the detector bulk. In addition to that there will be secondary X-rays induced by those particles and gamma rays hitting surrounding materials, also producing events far from detector center. The majority of events initiated by high energy particle background will have amplitude that is much higher than the X-ray events within the nominal range of NICER. Such events can be rejected by amplitude selection, and do not present a problem. But there will be a subset of events whose amplitude is within the nominal range, and those are more difficult to identify. We have established early in the program that X-ray events that originate far from the detector center have longer rise times (see [8]), and that presents a way to reject such events.

As described in section 2.2.2, the MPU has fast and slow chains analyzing in parallel the same signal coming from the detector. The slow chain peaking time of 465 ns remains much longer than the rise time even for events remote from detector center (at 2 mm away from center we measured rise time to be approximately 60 ns), and, as a result, slow chain amplitude does not depend on the event position. This is not true for the fast chain - the amplitude gets smaller as photon interaction occurs farther away and the signal rise time becomes comparable with the 84 ns peaking time and ballistic deficit [3] plays a bigger role. Thus, the ratio of fast/slow amplitudes for a given event can be used to reject events originating outside the 2 mm diameter of the detector collimator. Tests confirming validity of this approach were run with a function generator attached to the signal input of the MPU, feeding to the MPU voltage steps of the same amplitude as 4510 eV X-ray, but with variable rise time. A plot of the ratio of the amplitudes as a function of signal rise time is shown in Fig. 14 on the left. Error bars on the plot are much smaller than the symbol size, clearly indicating that discrimination of the events by the length of the rising edge works very well.

Direct tests with X-rays confirmed this result. On the right side of the Fig. 14 is a plot of fast/slow ratio for a positional scan across the detector. In this experiment an electron-impact X-ray source with Titanium target (4510 eV) illuminated the detector through a 100 micron pinhole, and the detector was scanned across the pinhole. In these tests a detector from the flight lot without a collimator was used to allow exposure of the remote portions of the detector surface. Preliminary scans were made to find the position of the detector center, so that the final scan (shown in the plot) would be centered. Again, statistical error bars are very small here.

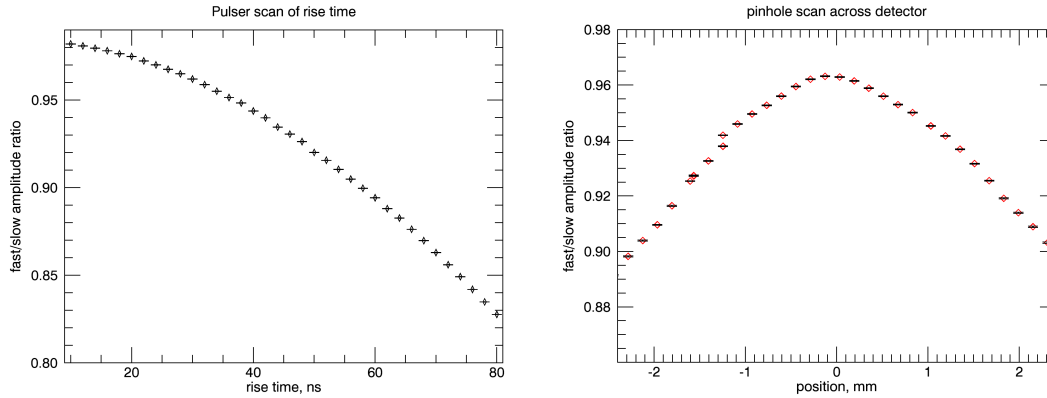


Figure 14. Left: a pulser scan with variable rise time shows fast/slow amplitude ratio as a function of rise time. Right: moving a small X-ray illuminated spot across the SDD illustrates that fast/slow amplitude ratio can help in rejecting events outside a given radius.

While the change in the ratio is small, it is possible to select a boundary value that would reject events outside a given radius. Such selection works reasonably well at higher energies, but becomes progressively worse at X-ray energies below 1.5 keV. We are planning additional experiments to investigate that region in greater detail.

4. CONCLUSION

NICER instrument, as we have shown above, is capable of providing excellent time resolution in conjunction with good spectroscopic performance, and that puts it in position to open a new window in X-ray astronomy.

ACKNOWLEDGMENTS

This work was funded by NASA contract NNG14PJ13C.

REFERENCES

- [1] Gendreau, K. et al., “The neutron star interior composition explorer (NICER): design and development,” *Proc SPIE*, **9905** (2016).
- [2] <http://amptek.com/products/fast-sdd-silicon-drift-detector/>.
- [3] Loo, B., Goulding, F., and Gao, D., “Ballistic deficit in pulse shaping amplifiers,” *IEEE Transaction on Nuclear Science* **35**, 114–118 (1998).
- [4] Gendreau, K., Arzoumanian, Z., Kenyon, S., and Spartana, N., “Miniaturized high-speed modulated X-ray source,” (US Patent 9,117,622 B2, 2015).
- [5] Beckhoff, B., Gottwald, A., Klein, R., Krumrey, M., Mller, R., Richter, M., Scholze, F., Thornagel, R., and Ulm, G., “A quarter-century of metrology using synchrotron radiation by PTB in Berlin,” *Physica Status Solidi, B* **246**, 1415–1434 (2009).
- [6] Gottwald, A., Kroth, U., Krumrey, M., Richter, M., Scholze, F., and Ulm, G., “The PTB high-accuracy spectral responsivity scale in the VUV and X-ray range,” *Metrologia* **43**, S125–S129 (2006).
- [7] Groom, D., Bebek, C., Fabricius, M., Karcher, A., Kolbe, W., Roe, N., and Steckert, J., “Quantum efficiency characterization of LBNL CCD’s. Part 1: the Quantum Efficiency machine,” *Proc. SPIE* **6068** (2006).
- [8] Prigozhin, G., Gendreau, K., Foster, R., Ricker, G., Villasenor, J., Doty, J., Kenyon, S., Arzoumanian, Z., Redus, R., and Huber, A., “Characterization of the silicon drift detector for NICER instrument,” *Proc SPIE* **8453** (2014).